

# Ligand and Anion Co-Leaching Induced Complete Reconstruction of Polyoxomolybdate-Organic Complex Oxygen-Evolving Pre-Catalysts

Xiong Liu, Fanjie Xia, Ruiting Guo, Meng Huang, Jiashen Meng, Jinsong Wu, and Liqiang Mai\*

The coordination compounds in the oxygen evolution reaction (OER) have been researched extensively. However, their poor durability (mostly < 100 h) and controversial reconstruction mechanism restrict their practical applications. Herein, a new-type polyoxomolybdate-organic complex (POMo) via wet-chemistry synthesis with fixed coordination between metal centers ( $\text{Ni}^{2+}$  and  $[\text{Mo}_8\text{O}_{26}]^{4-}$ ) and 2-Methylimidazole ligand is introduced. After introducing iron, a series of Fe-doped Ni-POMo with porous and amorphous structures are fabricated. These features accelerate the diffusion-leaching processes of ligands and anions, resulting in rapid and complete phase reconstruction during alkaline OER. As a result, nickel-iron (oxy)hydroxides with rich vacancies and poly-/low-crystalline features are in situ generated through dissolution-redeposition, and serve as the OER-active species. The optimized  $\text{Fe}_{0.052}\text{Ni-POMo}$  array pre-catalyst has excellent activity and sustains ultrastable catalysis for 545 h. The complete reconstruction of POMo enables high catalytic durability (230 h) and stable active phase under realistic conditions (30 wt% KOH, 60.9 °C). Accordingly, the completely reconstructed catalysts with unique structures and ultrastable catalysis have the potential to be applied in industry.

species.<sup>[6]</sup> These in situ techniques mainly include X-ray absorption spectroscopy,<sup>[7,8]</sup> X-ray diffraction (XRD),<sup>[9]</sup> Raman,<sup>[10–12]</sup> transmission electron microscopy (TEM),<sup>[13]</sup> electrochemistry-mass spectrometry,<sup>[14]</sup> and ultraviolet–visible spectroscopy (UV–vis).<sup>[15]</sup> Dynamic reconstruction processes of the catalyst have been revealed under working conditions, and the reconstructed species are commonly recognized as actual contributors in electrocatalysis.<sup>[16,17]</sup> OER is a fundamental reaction in diverse applications such as water electrolysis<sup>[13]</sup> and metal-air batteries.<sup>[18]</sup> However, its sluggish kinetics caused by multistep four-electron reaction remain a key issue in current researches.<sup>[19]</sup> Numerous OER electrocatalysts have been reported with surface reconstruction in the initial stage of electrochemical activation, which could be reflected by dynamically evolving cyclic voltammetry (CV) or chronopotentiometric curves and suggests a change in the pristine catalysts or active centers.<sup>[16,19–23]</sup>

## 1. Introduction

Recently, reconstruction-involved electrocatalysis has received much attention, including oxygen/hydrogen evolution reaction (OER/HER),<sup>[1–3]</sup> CO/CO<sub>2</sub> reduction<sup>[4,5]</sup> and so on. The development of advanced in situ techniques has impelled the in-depth understanding of intrinsic catalytic mechanism and real active

Nevertheless, the investigations of dynamic reconstruction processes and actual catalytic contributors still require further researches.

Due to their structural tunability and diverse chemical properties,<sup>[24]</sup> metal coordination compounds including mainstream metal-organic frameworks (MOFs) have received extensive researches on their direct applications in OER. The reconstruction degree after OER catalysis and catalytic durability of these materials are summarized (**Figure 1a**). Non-reconstruction phenomenon and no generation of new species have been observed in some robust coordination compounds.<sup>[25–31]</sup> For instance, Lang et al. discovered unchanged Fe/Ni/Co-based trimetallic Fe/Ni<sub>2.4</sub>/Co<sub>0.4</sub>-MIL-53 (MIL: Material of Institute Lavoisier) after 60 h-chronoamperometry operation.<sup>[30]</sup> Other reported metal coordination compounds are able to undergo partial<sup>[32–39]</sup> or even complete<sup>[40–45]</sup> reconstruction, and thus these compounds should be considered as pre-catalysts.<sup>[17]</sup> Therefore, there is no definitive answer as to whether reconstruction of coordination compounds would occur during electrocatalysis. For these reconstruction-involved pre-catalysts, the catalytic performance is positively correlated with the number of the reconstructed species, which provide real active sites. Hence,

X. Liu, F. Xia, R. Guo, M. Huang, Dr. J. Meng, Prof. J. Wu, Prof. L. Mai  
State Key Laboratory of Advanced Technology for Materials Synthesis  
and Processing

Wuhan University of Technology  
Wuhan 430070, China  
E-mail: mlq518@whut.edu.cn

Prof. L. Mai  
Foshan Xianhu Laboratory of the Advanced Energy Science  
and Technology Guangdong Laboratory  
Xianhu Hydrogen Valley  
Foshan 528200, China

 The ORCID identification number(s) for the author(s) of this article can be found under <https://doi.org/10.1002/adfm.202101792>.

DOI: 10.1002/adfm.202101792

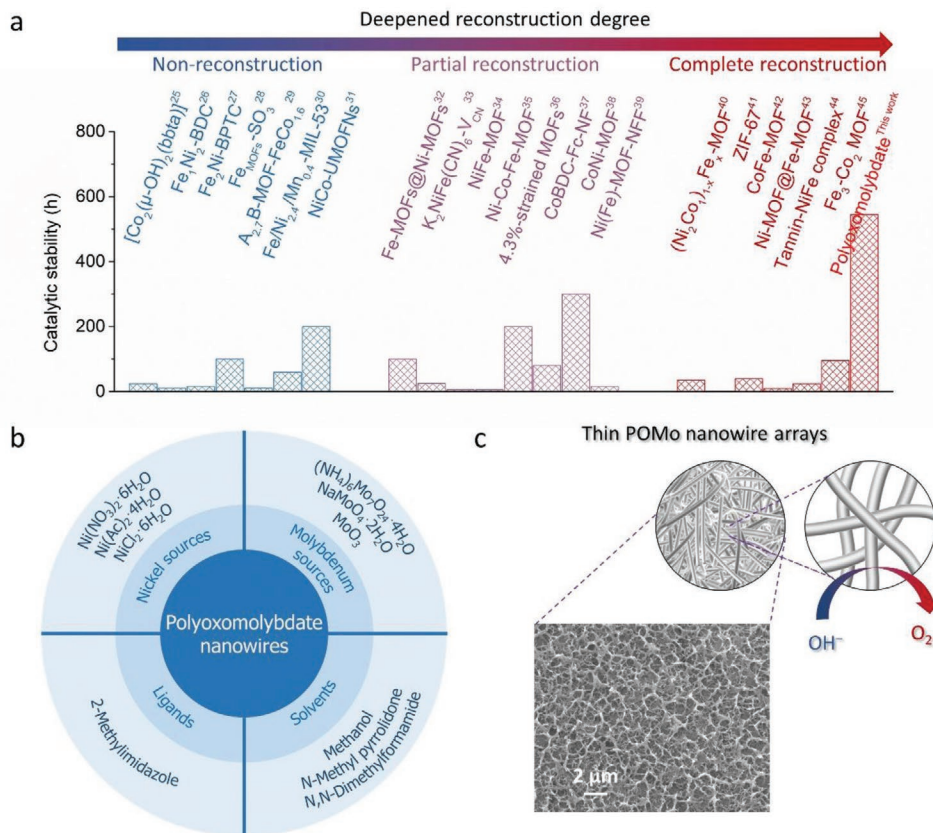


**Figure 1.** a) Summary of the reconstruction degree after OER catalysis and catalytic durability for reported coordination compounds and POMo in this work. b) Its fixed coordination mode in synthesizing Ni-POMo nanowires, which is independent of raw materials (nickel/molybdenum sources and solvents). c) Scanning electron microscopy image of Ni-POMo nanowire arrays and schematic diagram for OER catalysis.

complete reconstruction of the catalyst is supposed to produce more reconstructed species, but it is still a challenge to rationally design pre-catalysts which can be completely reconstructed. Another major issue is that the durability of these coordination compounds is currently less than 300 h, far below the requirement of industrial water electrolysis applications (>1000 h).<sup>[46]</sup> The harsh conditions, such as strong alkaline electrolytes (20–30 wt% KOH) and high temperatures (50–80 °C), are also required in industrial water electrolysis.<sup>[46,47]</sup> These harsh conditions may determine the reconstruction degree of coordination compounds and their intrinsic catalytic mechanism. Therefore, the performance evaluation and reconstruction study of the catalyst under industrial conditions are necessary and deserve attention.

Herein, in order to achieve complete reconstruction of the catalyst, the high-valence Mo species and ligand, which can easily leach out during OER, are introduced during synthesis of new-type organic–inorganic compounds. As a result, the synthesized nickel-based polyoxomolybdate-organic complex (Ni-POMo) via a facile wet-chemistry method displays low-crystalline and porous characteristics. The co-leaching of ligand and [Mo<sub>8</sub>O<sub>26</sub>]<sup>4-</sup> anion accelerates the structural crack and thus promotes the complete phase reconstruction of POMo, which results in the generation of (oxy)hydroxides with abundant defects. Combining in situ Raman with ex situ X-ray photoelectron spectroscopy (XPS) analysis, the reconstruction chemistry

and intrinsic catalytic mechanisms are uncovered. The obtained nickel-iron (oxy)hydroxide derived from Fe<sub>0.052</sub>Ni-POMo pre-catalyst displays optimized electrocatalytic performance. Furthermore, this work highlights the advantages of completely reconstructed catalyst derived from POMo pre-catalysts, such as unique structures (poly-/low-crystalline structure and rich grain boundaries) and ultrastable catalysis. The completely reconstructed catalyst can achieve high OER durability under realistic conditions (30 wt% KOH, 60.9 °C). Moreover, the active (oxy)hydroxide phase is well-remained after OER under harsh conditions.

## 2. Results and Discussion

Ni-POMo nanowires were fabricated by a facile solvothermal method involving the coordination reaction between organic ligand (2-Methylimidazole, denoted as 2-mim) and metal centers (Ni<sup>2+</sup> and [Mo<sub>8</sub>O<sub>26</sub>]<sup>4-</sup>), and the structure in POMo consists of the complex hydrogen-bonding between [Ni(2-mim)<sub>6</sub>]<sup>2+</sup> and [(2-mim)<sub>2</sub>Mo<sub>8</sub>O<sub>26</sub>]<sup>4-</sup>.<sup>[48,49]</sup> Though different nickel/molybdenum sources or different solvents were used during synthesis (Figure 1b), the obtained POMo products show nanowire morphology and similar Mo/Ni atomic ratios (Figure S1 and Table S1, Supporting Information). It suggests the fixed reaction pathway of coordination processes between metal centers

( $\text{Ni}^{2+}$  and  $[\text{Mo}_8\text{O}_{26}]^{4-}$ ) and 2-mim ligand. This phenomenon has also been reported in other types of polyoxomolybdates.<sup>[48]</sup> In addition, these Ni-POMo nanowires could effectively grow on conductive substrates, such as carbon cloth<sup>[49]</sup> and nickel foam (Figure 1c). Therefore, these POMo arrays can be applied in binder-free alkaline OER catalysis as schematically illustrated in Figure 1c.

Due to the advanced NiFe-based oxygen evolving catalysis,<sup>[14]</sup> iron-containing raw material was introduced during synthesis to fabricate Fe-incorporated Ni-POMo. A series of experiments by adding different contents of iron nitrate were carried out. Based on the inductively coupled plasma atomic emission spectrometry (ICP-AES) analysis (Figure 2a), the Fe/Ni atomic ratios (denoted as Fe/Ni-AR) of these POMo products are 0, 0.036, 0.052, and 0.094, respectively. The corresponding products are referred as  $\text{Fe}_x\text{Ni-POMo}$  ( $x = 0, 0.036, 0.052, \text{ and } 0.094$ ). Though the iron element could be successfully introduced into Ni-POMo, its content is limited to  $\text{Fe/Ni-AR} \leq 0.052$  to maintain the nanowire morphology (Figure S2, Supporting Information). From high-angle annular dark-field scanning transmission electron microscope (HAADF-STEM) images, the  $\text{Fe}_x\text{Ni-POMo}$  ( $x = 0, 0.036, \text{ and } 0.052$ ) show nanowire structure (Figure 2b–d and Figure S3, Supporting Information). The  $\text{Fe}_{0.052}\text{Ni-POMo}$  nanowires show  $\approx 25$  nm in diameter, and exhibit nearly amorphous characteristic according to high-resolution TEM (HRTEM) analysis (Figure 2e). Two diffused and inconspicuous diffraction rings are observed in the corresponding selected area electron diffraction (SAED, Figure 2f). Such a result suggests the existence of localized and quite small crystallinity (closed to an amorphous structure),<sup>[26]</sup> which is consistent to the two broad XRD peaks observed for  $\text{Fe}_{0.052}\text{Ni-POMo}$ . As shown in Figure S4 (Supporting Information), the two XRD peaks are centered at  $75^\circ$  and  $27^\circ$ , which are similar to that

of Fe-free one in our previous work.<sup>[49]</sup> HAADF-STEM image and corresponding energy dispersive X-ray spectroscopy (EDS) mappings further suggest uniform distribution of Fe, Ni, Mo, C, N, and O elements (Figure 2g).

As shown in Figure S2 (Supporting Information), the morphology of POMo radically changes from nanowire to irregular one when the iron content is excessive. Such a change may be attributed to the large difference between the radius of nickel ions and iron ions ( $\text{Ni}^{2+}$ , 0.69 Å;  $\text{Fe}^{2+}$ , 0.75 Å for low-spin one and 0.92 Å for high-spin one). When the nickel source was replaced entirely with iron source, the obtained Fe-POMo shows irregular morphology and could not effectively grow on the nickel foam (Figure S5, Supporting Information). By contrast, only  $\text{Fe}_x\text{Ni-POMo}$  ( $x = 0, 0.036, \text{ and } 0.052$ ) samples could remain nanowire array structure, and all of them show low crystallinity (Figure S6, Supporting Information). In addition, the nanowires become a little deformed as the iron content increases.

Due to their diverse topological characteristics, polyoxometalates (POMs) have potential applications in catalysis, photochemistry, etc.<sup>[50]</sup> Although POMs and their derived catalysts have been reported in OER catalysis, they still have unsatisfactory activity and durability. The summary for OER performance based on POMs and their derived catalysts is listed in Table S2 (Supporting Information). For example, Song et al. reported a robust Dexter-Silverton polyoxometalate oxygen evolution catalyst,  $[\text{Co}_{6.8}\text{Ni}_{1.2}\text{W}_{12}\text{O}_{42}(\text{OH})_4(\text{H}_2\text{O})_8]$ .<sup>[51]</sup> When it was tested in 0.1 M KOH at room temperature, a high overpotential of 360 mV was required to achieve  $10 \text{ mA cm}^{-2}$  and the stability test time was only 10 h. It suggests the application of POMs in OER requires a further breakthrough in catalytic performance, in the respect of material itself or its derivatives. POMo, one important subclass of POMs,<sup>[48]</sup> has not been reported to directly serve as OER

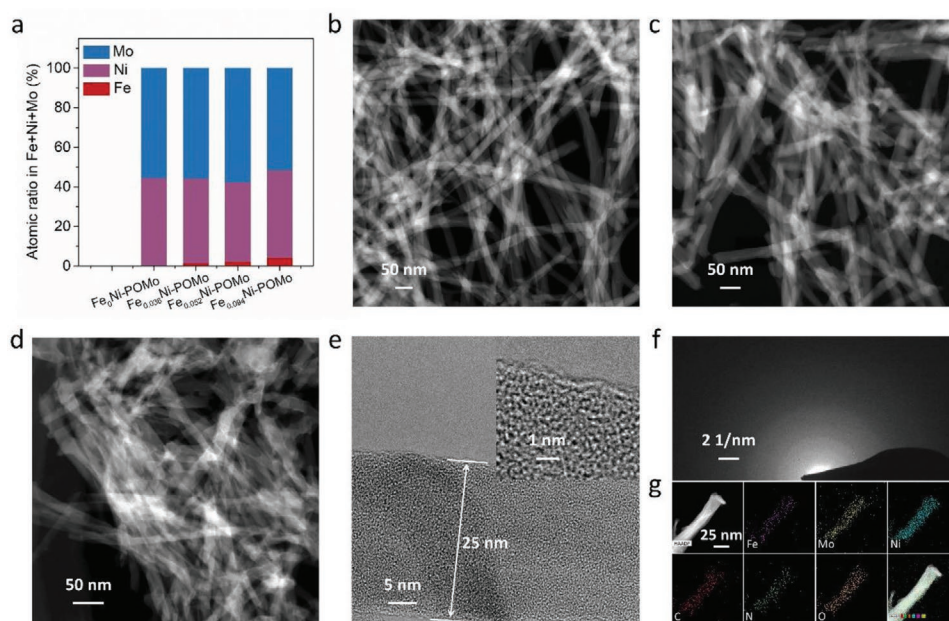


**Figure 2.** a) Component atomic ratio variation of  $\text{Fe}_x\text{Ni-POMo}$  ( $x = 0, 0.036, 0.052, \text{ and } 0.094$ ) from ICP-AES results. b–d) HAADF-STEM images of  $\text{Fe}_x\text{Ni-POMo}$  ( $x = 0, 0.036, \text{ and } 0.052$ ) nanowires, respectively. e) HRTEM images of single  $\text{Fe}_{0.052}\text{Ni-POMo}$  nanowire. f) SAED pattern of  $\text{Fe}_{0.052}\text{Ni-POMo}$  nanowires. g) HAADF-STEM image and the corresponding EDS mappings of  $\text{Fe}_{0.052}\text{Ni-POMo}$ .

catalysts. Herein, the electrocatalytic properties of  $\text{Fe}_x\text{Ni-POMo}$  ( $x = 0, 0.036, 0.052, \text{ and } 0.094$ ) for alkaline OER were investigated in a typical three-electrode system in 1 M KOH at room temperature. CV techniques were firstly adopted to activate  $\text{Fe}_x\text{Ni-POMo}$  prior to the OER measurements. As shown in Figure S7 (Supporting Information), the currents of newly formed oxidation peak ( $\text{Ni}^{2+} \rightarrow \text{Ni}^{3+}$ ) and that in OER regions gradually increase to stable values during 2 to 30-cycle CV. This implies the more exposure of new catalytic species and accessible sites for redox reaction during the initial CV tests. Similar electrochemical behaviors in inorganic pre-catalysts have also been reported by Song<sup>[16]</sup> and Hu<sup>[20]</sup> groups. Combined

with reconstruction mechanism analyses of POMo hereinafter,  $\text{Fe}_x\text{Ni-POMo}$  materials are considered as pre-catalysts, and their dynamic phase reconstruction to Ni(Fe) (oxy)hydroxides happens in the initial electrochemical activation.

The 30<sup>th</sup>-cycle CV curves of  $\text{Fe}_x\text{Ni-POMo}$  pre-catalysts are displayed in Figure 3a, which reflect enhanced OER activity after incorporating iron in Ni-POMo. All  $\text{Fe}_x\text{Ni-POMo}$  samples display obvious redox peaks, while the peak area decreases and the redox potentials are positively shifted after iron incorporation (Figure 3b). To evaluate the catalytic activities of  $\text{Fe}_x\text{Ni-POMo}$  pre-catalysts after CV activation, linear sweep voltammetry (LSV) measurements were carried out at a slow scan of  $2 \text{ mV s}^{-1}$ . All

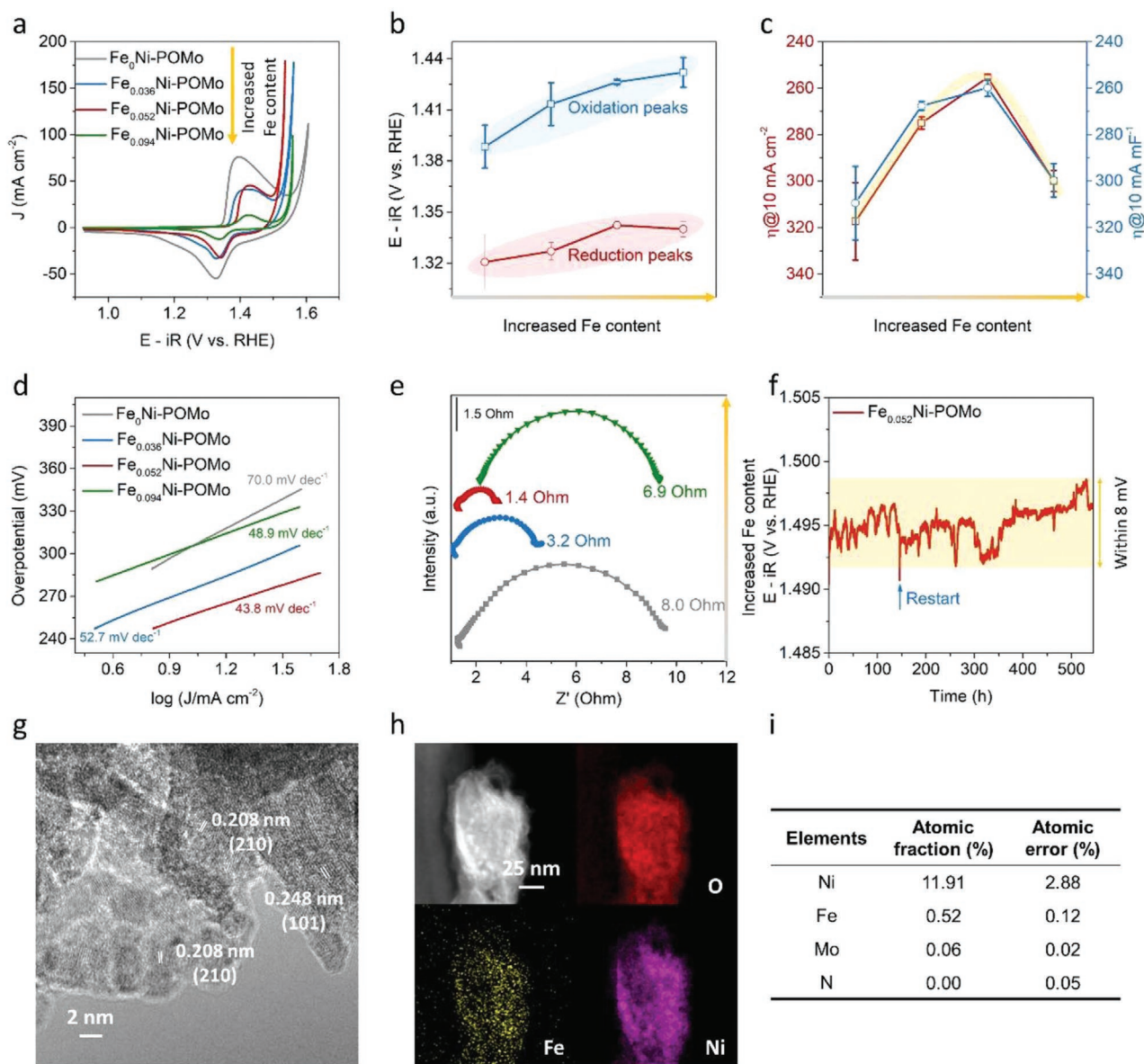


**Figure 3.** OER performance in 1 M KOH at room temperature. a) CV curves of  $\text{Fe}_x\text{Ni-POMo}$  ( $x = 0, 0.036, 0.052, 0.094$ ) arrays at  $50 \text{ mV s}^{-1}$ . b) The centered potentials of redox peaks for  $\text{Fe}_x\text{Ni-POMo}$  samples, which are obtained from their CV curves. c) Overpotentials at  $10 \text{ mA cm}^{-2}$  and  $10 \text{ mA mF}^{-1}$ , which are obtained from LSV curves of  $\text{Fe}_x\text{Ni-POMo}$  normalized by geometric area and ECSA, respectively. d, e) Tafel plots and Nyquist plots of  $\text{Fe}_x\text{Ni-POMo}$ , respectively. f) The prolonged chronopotentiometric response of  $\text{Fe}_{0.052}\text{Ni-POMo}$  at  $10 \text{ mA cm}^{-2}$ . g) HRTEM, h) HAADF-STEM images and the corresponding elemental mappings, and i) EDS results of elemental content of  $\text{Fe}_{0.052}\text{Ni-POMo}$  after OER.

the LSV data are iR-corrected and normalized by geometric area (GA) or electrochemical active surface area (ECSA). As displayed in the representative LSV curves of Fe<sub>x</sub>Ni-POMo (Figure S8, Supporting Information), the overpotentials by the function of Fe content present in a volcano-like fashion (Figure 3c). The Fe<sub>0.052</sub>Ni-POMo achieves the optimal catalytic performance with the lowest overpotential of 255.3 ± 1.6 mV at 10 mA cm<sup>-2</sup> ( $\eta_{10, GA}$ ) and 259.9 ± 3.7 mV at 10 mA mF<sup>-1</sup> ( $\eta_{10, ECSA}$ ), which are lower than that of Fe<sub>0</sub>Ni-POMo and Fe<sub>0.036</sub>Ni-POMo. However, with a higher iron content, the  $\eta_{10, GA}$  and  $\eta_{10, ECSA}$  values of Fe<sub>0.094</sub>Ni-POMo catalyst increase. Tafel slope derived from the polarization curves is an important parameter to describe the intrinsic OER kinetics.<sup>[20,26]</sup> In Figure 3d, the Fe-doped Ni-POMo catalysts show a significant decrease in Tafel slope when compared with Fe<sub>0</sub>Ni-POMo (70.0 mV dec<sup>-1</sup>), demonstrating superior OER kinetics of NiFe-based catalysts. Besides, the optimal Fe<sub>0.052</sub>Ni-POMo displays the Tafel slope close to 40 mV dec<sup>-1</sup>, indicating that a second electron transfer is involved as a rate-determining step in the electrochemical oxidation steps.<sup>[52]</sup> Electrochemical impedance spectroscopy (EIS) measurements were then operated to investigate the underlying factors of catalytic activity. The Fe-doped Ni-POMo catalysts exhibit decreased charge transfer resistances ( $R_{ct}$ , Figure 3e, which are smaller than that of Fe-free one (8.0 Ω). Particularly, the Fe<sub>0.052</sub>Ni-POMo shows the smallest  $R_{ct}$  value of only 1.4 Ω. Hence, the Fe dopant can greatly promote the charge transfer of NiOOH during OER processes. Fe-incorporated NiOOH has been reported to have over an order of magnitude higher conductivity than that of pure NiOOH, and Fe could exert a partial-charge transfer activation effect on Ni.<sup>[53]</sup> Therefore, the nickel-iron (oxy)hydroxide derived from nickel-iron POMo exhibits higher activity than the Fe-free one in this work. In addition, the suitable amount of Fe dopant, on one hand, can keep the nanowire morphology and microstructure of the precursor; on the other hand, it can form multi-metallic species with tuned electronic structure and optimized binding energy of surface oxygen intermediates.<sup>[52]</sup> Therefore, the optimized Fe<sub>0.052</sub>Ni-POMo locates at the top of volcano-like activity trend, which is associated with iron content.

Long-term OER stability of Ni-POMo and Fe<sub>0.052</sub>Ni-POMo was evaluated via a chronopotentiometric test at 10 mA cm<sup>-2</sup> (Figure 3f). For Ni-POMo, the potential to achieve a current density of 10 mA cm<sup>-2</sup> changes a little for at least 350 h (Figure S9, Supporting Information), which suggests that the reconstructed NiOOH derived from Ni-POMo can serve as stable OER-active species. For Fe<sub>0.052</sub>Ni-POMo, its recorded potentials display a negligible attenuation over a period of 545 h and the potential fluctuation is within 8 mV, which is expected to satisfy the industrial durability parameter (>1000 h).<sup>[46]</sup> In addition, the introduction of iron guarantees much enhanced OER activity with remained catalytic stability. The good catalytic durability makes Fe<sub>0.052</sub>Ni-POMo attractive as an advanced OER pre-catalyst among the reported POM and its derived catalysts (Table S2, Supporting Information). The characterization of products after long-term electrocatalysis is of great significance for the identification of catalytic active species. Different from the amorphous Fe<sub>0.052</sub>Ni-POMo pre-catalyst, its post-OER one exhibits low crystallinity (Figure 3g). The observed lattice spacings of 0.208 and 0.248 nm could be assigned to the (210) and

(101) planes of NiOOH (JCPDS, No. 27–956), respectively. The HAADF-STEM image and the corresponding elemental mappings indicate the uniform distribution of Ni, Fe, and O elements in the reconstructed catalyst (Figure 3h). Further EDS results confirm the nearly complete leaching of Mo and N species from the Fe<sub>0.052</sub>Ni-POMo pre-catalyst after OER (Figure 3i). The Mo/Ni atomic ratio is 0.005, suggesting the negligible Mo species in the reconstructed catalyst. Because the N species come from 2-Methylimidazole ligand, it can be concluded that the Fe<sub>0.052</sub>Ni-POMo undergoes the co-leaching of ligand and Mo species during OER. Finally, the completely reconstructed catalyst (i.e., nickel-iron (oxy)hydroxide) is in situ formed. The atomic ratio of iron to nickel in the reconstructed nickel-iron (oxy)hydroxide is determined as ≈0.044, which is a little bit smaller than that in the pristine Fe<sub>0.052</sub>Ni-POMo. The loss of iron may be attributed to partial iron leaching into the solution during reconstruction. The phenomenon of iron loss during OER also occurred in reported NiFe layered double hydroxide (NiFe-LDH) catalyst, and this would cause the activity decay.<sup>[54]</sup> Hence, there is some decrease in the activity of our completely reconstructed catalyst during stability tests.

Investigations on the dynamic evolution of pre-catalysts under working operation are helpful to understand the reconstruction mechanism and reveal the actual contributors in electrocatalysis. In situ electrochemistry-Raman measurements were conducted, providing the potential-dependent Raman spectra with in situ recorded polarization curve. During in situ Raman tests, the applied potentials are within 0.924–1.689 V versus reversible hydrogen electrode (denoted as  $V_{RHE}$ ), and the potential interval  $\Delta V$  is 30 mV. The recorded LSV curve is displayed in Figure S10 (Supporting Information). As shown in Figure 4a, no Raman peaks are found for the pristine Fe<sub>0.052</sub>Ni-POMo catalysts. At 1.554  $V_{RHE}$ , two Raman peaks centered at 474 and 554 cm<sup>-1</sup> appear, which can be assigned to the representative Ni-O vibrations of NiOOH.<sup>[15]</sup> The new Raman peaks are well-remained as the voltage bias increases. These observations indicate the formation of electro-oxidation induced nickel-iron (oxy)hydroxide, which is an electrochemically stable phase and serves as OER-active species. Ex situ Raman spectra for all Fe<sub>x</sub>Ni-POMo pre-catalysts also confirm the formation of OER-active (oxy)hydroxides (Figure 4b), which serve as the real catalytic species.

XPS was carried out to further understand the catalytic reconstruction mechanism and the change of elemental valence state of Fe<sub>0.052</sub>Ni-POMo during OER (Figure 4c–f and Figure S11; Supporting Information). Data collections of three stages were operated, including the pristine Fe<sub>0.052</sub>Ni-POMo, the activation sample after 30-cycle CV, and the post-OER sample after 500 h testing. The disappearance of Mo 3d and N 1s peaks after OER is observed, consistent with the electron microscopy results, and further confirm the co-leaching of ligand and anion. For Ni 2p and Fe 2p, both peaks shift positively after OER activation and then remain unchanged after 500 h test, confirming the formation of high-valence Ni/Fe species and the good stability property of the catalyst, respectively. Zhang et al. also reported similar XPS results of Ni 2p and Fe 2p and phase transformation when Ni-Co-Fe MOF served as OER pre-catalyst.<sup>[40]</sup> These results imply that the component stability of coordination compounds needs to be considered when they act as OER catalysts,

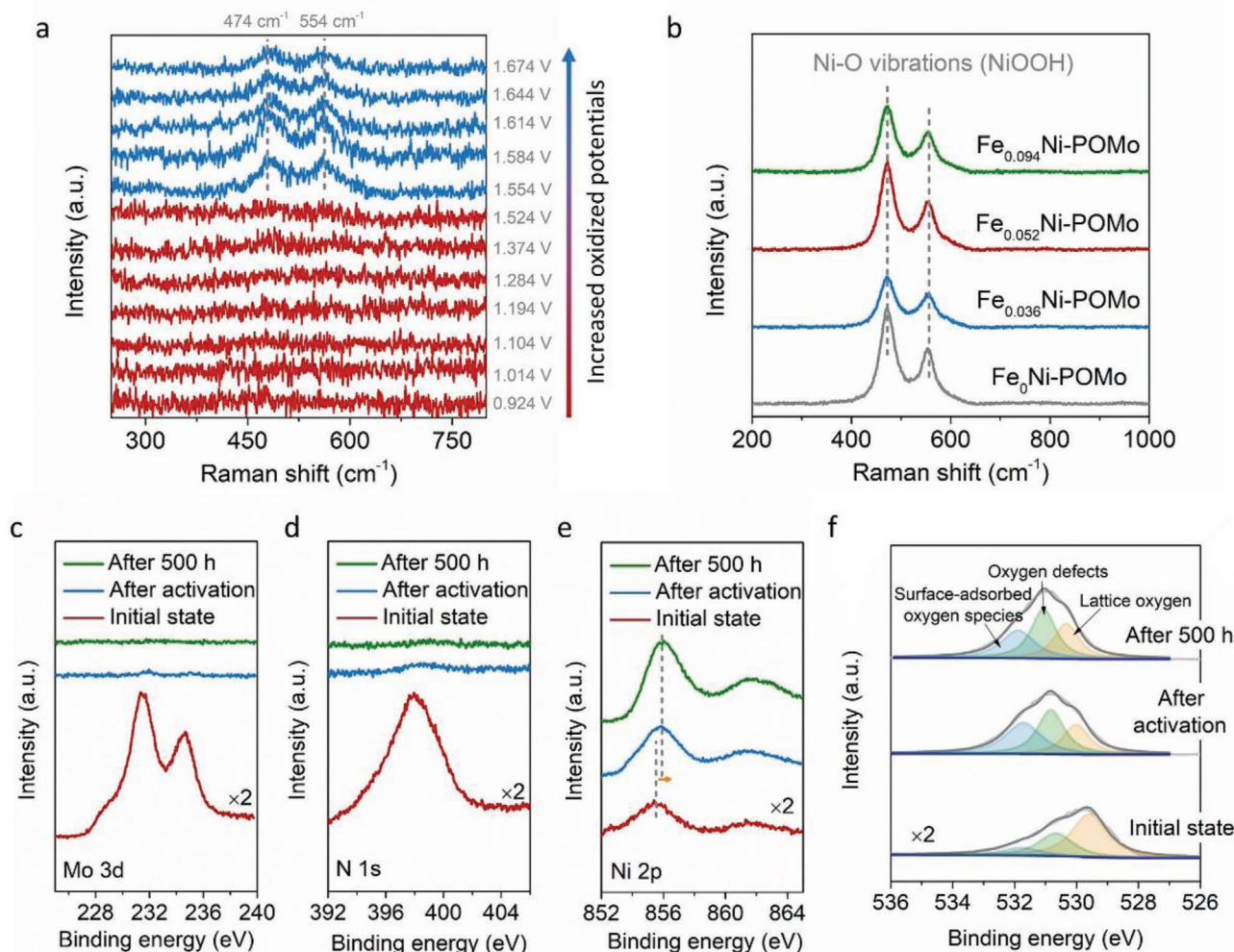


**Figure 4.** Activation mechanism and intrinsic catalytic active species. a) Potential-dependent in situ Raman of  $\text{Fe}_{0.052}\text{Ni-POMo}$  in 1 M KOH. b) Ex situ Raman spectra of  $\text{Fe}_x\text{Ni-POMo}$  after CV activation. c) Mo 3d, d) N 1s, e) Ni 2p, and f) O 1s XPS spectra of  $\text{Fe}_{0.052}\text{Ni-POMo}$  initially, after CV activation, and after OER for 500 h.

because it determines the actual catalytic species and catalytic mechanisms. Furthermore, O 1s XPS data confirm that there exists large content of O-vacancies in post-OER catalysts, which is attributed to the rapid reconstruction process and is beneficial for catalytic reaction.<sup>[55]</sup>

It raises a curiousness on the reasons for the complete reconstruction of  $\text{Fe}_x\text{Ni-POMo}$ . In fact, in the case of coordination compounds, the reconstruction phenomena commonly exist during OER because of their self-instability and the missing of ligand.<sup>[33,37,44]</sup> Some of them display partial reconstruction with limited phase evolution. Because the reconstructed species provide real and highly active catalytic sites, complete reconstruction is thus expected to occur for those coordination compounds to perform better. In our previous works, high-valence Mo species were confirmed to be soluble in alkaline solution in the form of molybdate ion.<sup>[12,21]</sup> Therefore, we designed this new Mo-containing coordination compound, i.e.,  $\text{Fe}_x\text{Ni-POMo}$ , to promote the phase evolution. For the designed POMo material, there exists the co-leaching of ligand and the high-valence Mo species, which are responsible for its complete reconstruction.

As shown in Figure S12a (Supporting Information), the elemental content in solution after soaking  $\text{Fe}_{0.052}\text{Ni-POMo}$  arrays in 1 M KOH was measured. The Mo/K molar ratio (0.547) is much higher than that of Ni/K (0.0259) and Fe/K (0.0175). Similar phenomenon has also been confirmed during the following electrochemical OER process. CV measurements were carried out in 0–0.8 V versus Hg/HgO at 50 mV s<sup>-1</sup> in 1 M KOH, and the solution was taken out for ICP-AES tests at various test stages. As shown in Figure S12b (Supporting Information), the Mo/K molar ratio increases with prolonging the electrochemical cycle time, while the Ni/K and Fe/K molar ratios change negligibly. These results suggest the inherent instability of POMo in alkaline solution, which is probably caused by the leaching of a large number of Mo-species during both chemical and electrochemical processes. As confirmed by various ex situ characterizations, the 2-mim ligand in POMo also completely leaches out. These massive leaches of species cause rapid, serious, and complete collapse of POMo, and the nickel-iron (oxy)hydroxides are thus in situ generated through a dissolution-redeposition way. Besides, numerous nanopores

could be directly observed from the HAADF-STEM images of  $\text{Fe}_x\text{Ni-POMo}$  ( $x = 0, 0.036, \text{ and } 0.052$ ) nanowires (Figure S6g–i, Supporting Information). These pores facilitate the mass transfer process in the reconstruction process, including electrolyte penetration and co-leaching of ligand and anion. Moreover, amorphous structure possesses good ion diffusion ability<sup>[55]</sup> for enhancing the co-leaching process. Hence, the nanoporous and low-crystalline structures and co-leaching processes drive the structural disintegration and complete reconstruction of POMo.

The reconstructed nickel-iron (oxy)hydroxides possess the characteristics of poly-/low-crystalline structures and rich grain boundaries (Figure S13a, Supporting Information). For comparison, we electrodeposited NiFe-LDH on the nickel foam. The activated NiFe-LDH possesses relatively higher crystallinity but no abundant facet orientation (Figure S13b, Supporting Information). The lower crystalline property of activated  $\text{Fe}_{0.052}\text{Ni-POMo}$  than that of activated NiFe-LDH could also be revealed by SAED patterns (Figure S13c,d, Supporting Information), because the former displays a more diffuse diffraction ring. OER activities of these two samples were evaluated in 1 M KOH at room temperature, and the obtained LSV curves were normalized by ECSA (Figure S13e, Supporting Information). To achieve  $10 \text{ mA mF}^{-1}$ , the overpotential of activated  $\text{Fe}_{0.052}\text{Ni-POMo}$  is 51 mV lower than that of the activated NiFe-LDH. Therefore, the unique structure of reconstructed nickel-iron (oxy)hydroxide is responsible for the high OER activity of  $\text{Fe}_{0.052}\text{Ni-POMo}$ .

It is important to evaluate the performance of catalysts under industrial parameters. However, there is a gap in evaluating catalyst performance between current studies and industrial conditions (Figure 5a). To confirm the advantages of the completely reconstructed catalyst in this work, we evaluated its OER performance via chronopotentiometric measurements in 30 wt% KOH at  $60.9^\circ\text{C}$ . As shown in Figure 5b, the nickel-iron (oxy)hydroxide, which is completely reconstructed from  $\text{Fe}_{0.052}\text{Ni-POMo}$ , exhibits stable OER for 230 h with small potential fluctuation of  $\approx 60 \text{ mV}$ . Nickel metal is one of the commonly used electrode materials in commercial water electrolysis system,<sup>[56]</sup> while it shows high OER overpotentials and rapid decay of activity during 90 h-OER operation. Hence, the  $\text{Fe}_{0.052}\text{Ni-POMo}$  electrode can serve as one of the candidates for water electrolysis application. Raman spectrum of nickel-iron (oxy)hydroxide after OER shows two peaks, which are similar to the original

one (Figure 5c). These results demonstrate the good catalytic stability and stable active phase of the completely reconstructed catalyst under harsh conditions. Currently, the conditions for catalytic performance evaluation in laboratory are far less stringent than that in industry. Therefore, it is necessary to consider the component stability of coordination compounds under widely demanding conditions. Herein, although the real OER-active contributors are based on the reconstructed catalyst but not the original POMo material, the completely reconstructed one is featured by unique structures (poly-/low-crystalline structure and rich grain boundaries) and can achieve higher catalytic activity and better stability. Therefore, the completely reconstructed catalyst proposed in this work is expected to be applied to meet the industrial requirements.

### 3. Conclusion

In conclusion, we have developed a facile wet-chemistry method for directly growing  $\text{Fe}_x\text{Ni-POMo}$  nanowires with a controlled amount of iron on the nickel foam. The fixed coordination between metal centers ( $\text{Ni}^{2+}$  and  $[\text{Mo}_8\text{O}_{26}]^{4-}$ ) and 2-mim ligand enables the raw material-independent synthesis. In situ Raman and a series of ex situ characterizations confirm the complete reconstruction mechanism. The low-crystalline and porous features of POMo accelerate the diffusion-leaching processes of ligand and anion. Meanwhile, the applied oxidation potential promotes the formation of OER-active (oxy)hydroxide. The OER activities of  $\text{Fe}_x\text{Ni-POMo}$  pre-catalysts show a volcano-like trend, and the  $\text{Fe}_{0.052}\text{Ni-POMo}$  possesses the optimized catalytic performance with lowest overpotential and Tafel slope. Especially, the activity of  $\text{Fe}_{0.052}\text{Ni-POMo}$  maintains for 545 h in the durability test and the potential fluctuation is within 8 mV, showing its superior OER catalytic stability. The present work highlights the advantages of complete reconstruction of POMo pre-catalysts, which are essential for making stable active phase and durable catalysis under harsh conditions. In terms of stability test time, although there is still some distance from industrial parameters ( $> 1000 \text{ h}$ ), this work highlights the importance of evaluating performance against industrial parameters. This work promotes the basic understanding and practical application of coordination compounds in catalytic applications.

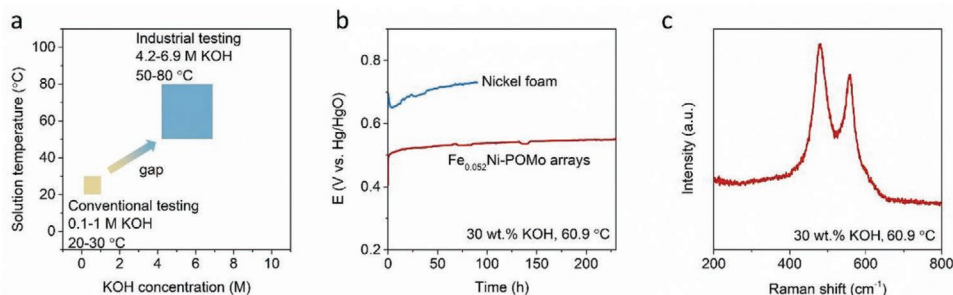


**Figure 5.** a) There is a certain gap between traditional test parameters and industrial test parameters. b) Chronopotentiometric response of  $\text{Fe}_{0.052}\text{Ni-POMo}$  pre-catalyst and pure nickel foam at  $10 \text{ mA cm}^{-2}$ . Here, the 30-cycle CV activation was firstly carried out before chronopotentiometric measurement of  $\text{Fe}_{0.052}\text{Ni-POMo}$ . c) Raman spectrum of  $\text{Fe}_{0.052}\text{Ni-POMo}$  after one-day OER measurement.

## Supporting Information

Supporting Information is available from the Wiley Online Library or from the author.

## Acknowledgements

X.L. and F.X. contributed equally to this work. This work was supported by the National Key Research and Development Program of China (2020YFA0715000), the National Natural Science Foundation of China (51521001), Foshan Xianhu Laboratory of the Advanced Energy Science and Technology Guangdong Laboratory (XHT2020-003). The S/TEM work was performed at the Nanostructure Research Center (NRC), supported by the Fundamental Research Funds for the Central Universities (WUT: 2021111016GX).

## Conflict of Interest

The authors declare no conflict of interest.

## Data Availability Statement

Research data are not shared.

## Keywords

complete reconstruction, in situ Raman, multi-component co-leaching, polyoxomolybdate-organic complexes, ultrastable oxygen evolution

Received: February 20, 2021

Published online:

- [1] C. Y. Hu, Q. Y. Ma, S.-F. Hung, Z.-N. Chen, D. H. Ou, B. Ren, H. M. Chen, G. Fu, N. F. Zheng, *Chem* **2017**, *3*, 122.
- [2] L. Q. He, W. B. Zhang, Q. J. Mo, W. J. Huang, L. C. Yang, Q. S. Gao, *Angew. Chem., Int. Ed.* **2020**, *59*, 3544.
- [3] E. Fabbri, M. Nachttegaal, T. Binninger, X. Cheng, B.-J. Kim, J. Durst, F. Bozza, T. Graule, R. Schäublin, L. Wiles, M. Pertoso, N. Danilovic, K. E. Ayers, T. J. Schmidt, *Nat. Mater.* **2017**, *16*, 925.
- [4] P. D. Luna, R. Quintero-Bermudez, C.-T. Dinh, M. B. Ross, O. S. Bushuyev, P. Todorović, T. Regier, S. O. Kelley, P. D. Yang, E. H. Sargent, *Nat. Catal.* **2018**, *1*, 103.
- [5] S. B. Scott, T. V. Hogg, A. T. Landers, T. Maagaard, E. Bertheussen, J. C. Lin, R. C. Davis, J. W. Beeman, D. Higgins, W. S. Drisdell, C. Hahn, A. Mehta, B. Seger, T. F. Jaramillo, I. Chorkendorff, *ACS Energy Lett.* **2019**, *4*, 803.
- [6] X. N. Li, H.-Y. Wang, H. B. Yang, W. Z. Cai, S. Liu, B. Liu, *Small Methods* **2018**, *2*, 1700395.
- [7] M. Kim, B. Lee, H. Ju, S. W. Lee, J. Kim, *Adv. Mater.* **2019**, *31*, 1901977.
- [8] T. Z. Wu, S. N. Sun, J. J. Song, S. B. Xi, Y. H. Du, B. Chen, W. A. Sasangka, H. B. Liao, C. L. Gan, G. G. Scherer, L. Zeng, H. J. Wang, H. Li, A. Grimaud, Z. C. J. Xu, *Nat. Catal.* **2019**, *2*, 763.
- [9] Z. H. Yan, H. M. Sun, X. Chen, H. H. Liu, Y. R. Zhao, H. X. Li, W. Xie, F. Y. Cheng, J. Chen, *Nat. Commun.* **2018**, *9*, 2373.
- [10] Y. Wang, Y. L. Zhu, S. L. Zhao, S. X. She, F. F. Zhang, Y. Chen, T. Williams, T. Gengenbach, L. H. Zu, H. Y. Mao, W. Zhou, Z. P. Shao, H. T. Wang, J. Tang, D. Y. Zhao, C. Selonulya, *Matter* **2020**, *3*, 2124.
- [11] X. Liu, K. Ni, B. Wen, R. T. Guo, C. J. Niu, J. S. Meng, Q. Li, P. J. Wu, Y. W. Zhu, X. J. Wu, L. Q. Mai, *ACS Energy Lett.* **2019**, *4*, 2585.
- [12] X. Liu, R. T. Guo, K. Ni, F. J. Xia, C. J. Niu, B. Wen, J. S. Meng, P. J. Wu, J. S. Wu, X. J. Wu, L. Q. Mai, *Adv. Mater.* **2020**, *32*, 2001136.
- [13] N. O. Peña, D. Ihiawakrim, M. Han, B. Lassalle-Kaiser, S. Carenco, C. Sanchez, C. Laberty-Robert, D. Portehault, O. Ersen, *ACS Nano* **2019**, *13*, 11372.
- [14] C. Roy, B. Sebok, S. B. Scott, E. M. Fiordaliso, J. E. Sørensen, A. Bodin, D. B. Trimarco, C. D. Damsgaard, P. C. K. Vesborg, O. Hansen, I. E. L. Stephens, J. Kibsgaard, I. Chorkendorff, *Nat. Catal.* **2018**, *1*, 820.
- [15] B. J. Trzeźniewski, O. Diaz-Morales, D. A. Vermaas, A. Longo, W. Bras, M. T. M. Koper, W. A. Smith, *J. Am. Chem. Soc.* **2015**, *137*, 15112.
- [16] H. L. Jiang, Q. He, X. Y. Li, X. Z. Su, Y. K. Zhang, S. M. Chen, S. Zhang, G. Z. Zhang, J. Jiang, Y. Luo, P. M. Ajayan, L. Song, *Adv. Mater.* **2019**, *31*, 1805127.
- [17] S. Jin, *ACS Energy Lett.* **2017**, *2*, 1937.
- [18] Y. G. Li, J. Lu, *ACS Energy Lett.* **2017**, *2*, 1370.
- [19] B. W. Zhang, K. Jiang, H. T. Wang, S. Hu, *Nano Lett.* **2019**, *19*, 530.
- [20] N. Clament Sagaya Selvam, L. J. Du, B. Y. Xia, P. J. Yoo, B. You, *Adv. Funct. Mater.* **2021**, *31*, 2008190.
- [21] X. Liu, J. S. Meng, K. Ni, R. T. Guo, F. J. Xia, J. J. Xie, X. Li, B. Wen, P. J. Wu, M. Li, J. S. Wu, X. J. Wu, L. Q. Mai, D. Y. Zhao, *Cell Rep. Phys. Sci.* **2020**, *4*, 100241.
- [22] H. L. Jiang, Q. He, Y. K. Zhang, L. Song, *Acc. Chem. Res.* **2018**, *51*, 2968.
- [23] Q. C. Xu, H. Jiang, X. Z. Duan, Z. Jiang, Y. J. Hu, S. W. Boettcher, W. Y. Zhang, S. J. Guo, C. Z. Li, *Nano Lett.* **2021**, *21*, 492.
- [24] H.-C. Zhou, J. R. Long, O. M. Yaghi, *Chem. Rev.* **2012**, *112*, 673.
- [25] X.-F. Lu, P.-Q. Liao, J.-W. Wang, J.-X. Wu, X.-W. Chen, C.-T. He, J.-P. Zhang, G.-R. Li, X.-M. Chen, *J. Am. Chem. Soc.* **2016**, *138*, 8336.
- [26] J. T. Li, W. Z. Huang, M. M. Wang, S. B. Xi, J. S. Meng, K. N. Zhao, J. Jin, W. W. Xu, Z. Y. Wang, X. Liu, Q. Chen, X. B. Liao, Y. L. Jiang, K. A. Owusu, B. L. Jiang, C. X. Chen, D. N. Fan, L. Zhou, L. Q. Mai, *ACS Energy Lett.* **2019**, *4*, 285.
- [27] X.-L. Wang, L.-Z. Dong, M. Qiao, Y.-J. Tang, J. Liu, Y. F. Li, S.-L. Li, J.-X. Su, Y.-Q. Lan, *Angew. Chem., Int. Ed.* **2018**, *57*, 9660.
- [28] K. Feng, D. Zhang, F. F. Liu, H. Li, J. B. Xu, Y. J. Xia, Y. Y. Li, H. P. Lin, S. A. Wang, M. W. Shao, Z. H. Kang, J. Zhong, *Adv. Energy Mater.* **2020**, *10*, 2000184.
- [29] Z. Q. Xue, Y. L. Li, Y. W. Zhang, W. Geng, B. M. Jia, J. Tang, S. X. Bao, H.-P. Wang, Y. N. Fan, Z.-W. Wei, Z. S. Zhang, Z. F. Ke, G. Q. Li, C.-Y. Su, *Adv. Energy Mater.* **2018**, *8*, 1801564.
- [30] F.-L. Li, Q. Shao, X. Q. Huang, J.-P. Lang, *Angew. Chem., Int. Ed.* **2018**, *57*, 1888.
- [31] S. L. Zhao, Y. Wang, J. C. Dong, C.-T. He, H. J. Yin, P. F. An, K. Zhao, X. F. Zhang, C. Gao, L. J. Zhang, J. W. Lv, J. X. Wang, J. Q. Zhang, A. M. Khattak, N. A. Khan, Z. X. Wei, J. Zhang, S. Q. Liu, H. J. Zhao, Z. Y. Tang, *Nat. Energy* **2016**, *1*, 16184.
- [32] M. Liu, L. J. Kong, X. M. Wang, J. He, X.-H. Bu, *Small* **2019**, *15*, 1903410.
- [33] Z.-Y. Yu, Y. Duan, J.-D. Liu, Y. Chen, X.-K. Liu, W. Liu, T. Ma, Y. Li, X.-S. Zheng, T. Yao, M.-R. Gao, J.-F. Zhu, B.-J. Ye, S.-H. Yu, *Nat. Commun.* **2019**, *10*, 2799.
- [34] J. J. Duan, S. Chen, C. Zhao, *Nat. Commun.* **2017**, *8*, 15341.
- [35] W. Ahn, M. G. Park, D. U. Lee, M. H. Seo, G. P. Jiang, Z. P. Cano, F. M. Hassan, Z. W. Chen, *Adv. Funct. Mater.* **2018**, *28*, 1802129.
- [36] W. R. Cheng, X. Zhao, H. Su, F. M. Tang, W. Che, H. Zhang, Q. H. Liu, *Nat. Energy* **2019**, *4*, 115.
- [37] Z. Q. Xue, K. Liu, Q. L. Liu, Y. L. Li, M. R. Li, C.-Y. Su, N. Ogiwara, H. Kobayashi, H. Kitagawa, M. Liu, G. Q. Li, *Nat. Commun.* **2019**, *10*, 5048.
- [38] L. Huang, G. Gao, H. Zhang, J. X. Chen, Y. X. Fang, S. J. Dong, *Nano Energy* **2020**, *68*, 104296.

- [39] C. S. Cao, D.-D. Ma, Q. Xu, X.-T. Wu, Q.-L. Zhu, *Adv. Funct. Mater.* **2018**, *29*, 1807418.
- [40] Q. Z. Qian, Y. P. Li, Y. Liu, L. Yu, G. Q. Zhang, *Adv. Mater.* **2019**, *31*, 1901139.
- [41] W. R. Zheng, M. J. Liu, L. Y. S. Lee, *ACS Catal.* **2020**, *10*, 81.
- [42] Z. H. Zou, T. T. Wang, X. H. Zhao, W.-J. Jiang, H. R. Pan, D. Q. Gao, C. L. Xu, *ACS Catal.* **2019**, *9*, 7356.
- [43] K. Rui, G. Q. Zhao, Y. P. Chen, Y. Lin, Q. Zhou, J. Y. Chen, J. X. Zhu, W. P. Sun, W. Huang, S. X. Dou, *Adv. Funct. Mater.* **2018**, *28*, 1801554.
- [44] Y. M. Shi, Y. Yu, Y. Liang, Y. H. Du, B. Zhang, *Angew. Chem., Int. Ed.* **2019**, *58*, 3769.
- [45] J.-Q. Shen, P.-Q. Liao, D.-D. Zhou, C.-T. He, J.-X. Wu, W.-X. Zhang, J.-P. Zhang, X.-M. Chen, *J. Am. Chem. Soc.* **2017**, *139*, 1778.
- [46] V. R. Stamenkovic, D. Strmcnik, P. P. Lopes, N. M. Markovic, *Nat. Mater.* **2017**, *16*, 57.
- [47] F. F. Guo, Y. Y. Wu, H. Chen, Y. P. Liu, L. Yang, X. Ai, X. X. Zou, *Energy Environ. Sci.* **2019**, *12*, 684.
- [48] M.-L. Cao, X.-L. Zhang, *J. Mol. Struct.* **2011**, *994*, 75.
- [49] X. Liu, K. Ni, B. Wen, C. J. Niu, J. S. Meng, R. T. Guo, Q. Li, J. T. Li, Y. W. Zhu, X. J. Wu, D. Y. Zhao, L. Q. Mai, *J. Mater. Chem. A* **2018**, *6*, 17874.
- [50] N. I. Gumerova, A. Rompel, *Nat. Rev. Chem.* **2018**, *2*, 0112.
- [51] W. J. Luo, J. Hu, H. L. Diao, B. Schwarz, C. Streb, Y.-F. Song, *Angew. Chem., Int. Ed.* **2017**, *56*, 4941.
- [52] Y. C. Pi, P. T. Wang, F. Lv, S. J. Guo, J. Guo, X. Q. Huang, *Angew. Chem., Int. Ed.* **2017**, *129*, 4573.
- [53] L. Trotochaud, S. L. Young, J. K. Ranney, S. W. Boettcher, *J. Am. Chem. Soc.* **2014**, *136*, 6744.
- [54] R. Chen, S. Hung, D. J. Zhou, J. J. Gao, C. J. Yang, H. B. Tao, H. B. Yang, L. P. Zhang, L. L. Zhang, Q. H. Xiong, H. M. Chen, B. Liu, *Adv. Mater.* **2019**, *31*, 1903909.
- [55] Y. Duan, Z.-Y. Yu, S.-J. Hu, X.-S. Zheng, C.-T. Zhang, H.-H. Ding, B.-C. Hu, Q.-Q. Fu, Z.-L. Yu, X. Zheng, J.-F. Zhu, M.-R. Gao, S.-H. Yu, *Angew. Chem., Int. Ed.* **2019**, *58*, 15772.
- [56] X. Y. Lu, J. Pan, E. Lovell, T. H. Tan, Y. H. Ng, R. Amal, *Energy Environ. Sci.* **2018**, *11*, 1898.